1995

Description and Vorticity Analysis of 50-Day Oscillations in the Western Tropical Region of the CME Model

Julie L. McClean

John M. Klinck
Old Dominion University, jklinck@odu.edu

Original Publication Citation

McClean, J.L., & Klinck, J.M. (1995). Description and vorticity analysis of 50-day oscillations in the western tropical region of the CME model. *Journal of Physical Oceanography, 25*(11), 2498-2517. doi: 10.1175/1520-0485(1995)0252.0.co;2

Description and Vorticity Analysis of 50-Day Oscillations in the Western Tropical Region of the CME Model

JULIE L. MCCLEAN

Department of Oceanography, Naval Postgraduate School, Monterey, California

JOHN M. KLINCK

Department of Oceanography, Old Dominion University, Norfolk, Virginia

(Manuscript received 20 December 1993, in final form 8 December 1994)

ABSTRACT

The WOCE Community Modeling Effort (CME) general circulation model of the North Atlantic was used to investigate the behavior, nature, and dynamics of 50-day oscillations seen in the meridional component of velocity between 5° and 11°N, 35° and 55°W. Oscillations of the meridional component of velocity, with a period of about 50 days, appear as the seasonal meander pattern of the North Equatorial Countercurrent starts to break down in December. They appear first near 35°W and are advected westward. They have a westward phase velocity of about 0.1 m s^{-1}, wavelength of about 600 km, and a very slow eastward group velocity. Their period, phase speed, and wavelength agree with recent observations. Calculation of the leading terms from the full vorticity equation following a modal decomposition in the propagation region showed that the oscillations were first and second mode baroclinic Rossby waves. Repetition of the vorticity analysis on an undecomposed snapshot during the period of the retroflection revealed the NECC meanders also to be baroclinic Rossby waves, the same as the 50-day oscillations. These findings, together with the time evolution of the individual flow components over an annual cycle, suggested that the 50-day oscillations were the westward advected residue of the NECC meander pattern that is released as the NECC slows in December. The retroflecting North Brazil Current produces Rossby waves with very slow eastward group velocity that are advected eastward by the NECC until they reach 35°W, where they dissipate. A standing wave pattern is established for several months, while the NECC is active. Once it slows, the waves are advected westward and disappear totally by May. Neither wind forcing nor barotropic instability were considered to be responsible for the oscillations in the model.

1. Introduction

Recently, oscillations of the meridional component of velocity, with a mean periodicity of about 50 days, have been observed in the western tropical Atlantic by Johns et al. (1990). These observations were obtained from current meter moorings that were deployed over the slope at 7.5°N, 53.7°W and in 5000 m of water at 8.5°N, 52.2°W, for about one year. The oscillations were present all year; however, their period varied from 40 to 60 days, with the shortest periods occurring in spring and the longest in fall. They were observed over the top 900 m of the water column with the strongest signature occurring at the upper current meter at 100-m depth. Peak-to-peak fluctuations in excess of 1 m s^{-1} were recorded. Variance-preserving spectra of the meridional velocity showed coherent peaks near 40–50 days. The narrowband nature of the signal lead Johns et al. (1990) to suggest that the oscillations arose from a single coherent wave process. From a cross-spectrum calculation, currents at the most westward site were found to lag behind those located to the east by about 6 days, in the 40–60 day band. If a wave is assumed to have propagated through the array, its wavelength is 520 km with a range of 390–740 km and its phase speed −0.12 m s^{-1} with a range of −0.09 to −0.17 m s^{-1}. These estimates were found to be consistent with the characteristics of off-equatorial first baroclinic mode Rossby waves.

Oscillations with periods of 50 days have also been observed south of the equator in the western Indian Ocean, a region dynamically similar to that of the North Brazil Current retroflection. In the latter region, both the North Brazil Current (NBC) and the North Equatorial Countercurrent (NECC) exhibit strong seasonal variability. In the fall, the NBC retroflects, or turns back on itself, to form the western arm of the eastward flowing meandering NECC. During the spring, the NECC is replaced by westward flow and the NBC continues northwestward along the coast of South America

Corresponding author address: Dr. Julie L. McClean, Department of Oceanography, Naval Postgraduate School, Monterey, CA 93943-5122.
E-mail: mcclean@oc.nps.navy.mil

toward the Caribbean (Richardson and McKee 1984). In the Indian Ocean, the South Equatorial Current (SEC) splits at the coast of Madagascar into northward and southward branches. During the northeast monsoon (November–March), the northward branch rounds the tip of Madagascar at 12°S and continues north along the coast of Africa as the East African Coastal Current (EACC). During this season, the Somali Current flows southward across the equator and joins the EACC off Kenya to form an eastward South Equatorial Countercurrent (SECC) (Swallow et al. 1988). Climatological mean surface currents for this period compiled from ship drift data, show this current to meander as it flows offshore (Swallow et al. 1991). During the southwest monsoon (May–September), the EACC flows into the northward flowing Somali Current.

Mysak and Mertz (1984) found 40–50 day oscillations in the longshore current and temperature fluctuations that were measured in the Somali Current source region at 3°S, 41°E off Kenya, from January to July 1976. They found similar period fluctuations in the zonal wind stress component collected at 2.5°S, 47.5°E during these months. The latter signal was the 40–50 day oscillation of the tropospheric wind field discovered by Madden and Julian (1972). Consequently, they attributed the oceanic oscillations to forcing by this atmospheric signal. The coupling mechanism was not understood. Alternatively, they suggested that since the Somali Current had strong lateral shears, the oscillations may be due to barotropic instability. Atmospheric forcing was also suggested by Quadfasel and Swallow (1986) as the cause of 50-day oscillations found off the northern tip of Madagascar in the South Equatorial Current (SEC) during March–July 1975. They did not, however, have any wind data to substantiate their claim. Later, Schott et al. (1988) found that the wind field in this region did not have a prominent peak in the 40–50 day period and instead, attributed the oscillations to shear instability of the zonal current system.

Kindle and Thompson (1989) found 50-day oscillations of the meridional velocity component in their reduced-gravity model of the western Indian Ocean between 3° and 8°S, west of 55°E. Realistic basin geometry north of 30°S was used, while the model was forced with Hellerman and Rosenstein (1983) monthly wind stress climatology. The oscillations initially appeared at 55°E where the meander pattern associated with the eastward-flowing offshore branch of the EACC first broke down. The onset of the oscillations and the break down of the meander pattern occurred almost coincidentally during April. The oscillations were seen near the coast of Africa (40°E) by mid-June. Westward flow also appeared at 55°E during April and then at progressively westward locations, until it was seen near the coast in June. As a result, Kindle and Thompson (1989) attributed the oscillations to barotropic instability. Wind forcing was not considered to be responsible since little wind energy was contained in the 40–60 day period in the model forcing. They also found these oscillations to have the character of first baroclinic mode Rossby waves.

Johns et al. (1990) have speculated as to the cause of the 50-day oscillations in the tropical Atlantic. They documented the shedding of an eddy from the retroflection region using coastal zone color scanner imagery. One possibility is that the oscillations seen in the current meter records are associated with the shedding of these eddies. A recent study by Didden and Schott (1993) investigated mesoscale fluctuations in the western tropical Atlantic using Geosat altimetry for the period November 1986 through June 1989, where they noted the detachment of anticyclonic eddies from the NBC during November–January. The eddies were traced for more than two months as they moved northwestward along South America toward the Caribbean, at average speeds of 0.15 m s^{-1}. They compared the occurrences of these eddies with the current meter records collected by Johns et al. (1990) and found that although the oscillations persisted throughout 1987–1988 in the current measurements near the retroflection zone, oniy those of winter 1987/88 were associated with eddies identifiable in the altimetric maps. They commented that the persistent 40–60 day background oscillations appear to exist independently of the retroflection; however, their interaction with the retroflection may cause the eddy shedding. Alternatively, Johns et al. (1990) suggested that the oscillations may result from the westward movement of the NECC meander pattern that is released when the NECC decays at the end of fall. In an attempt to better understand the dynamics of the oscillations, they examined output from the World Ocean Circulation Experiment (WOCE) Community Modeling Effort (CME) general circulation model, which is one of the most realistic calculations to date. No evidence of the oscillations or eddy shedding was found in the N13-1 experiment, the initial 25-year simulation discussed by Bryan et al. (1994). This could be due to the choice of the coefficients of vertical and horizontal diffusion, which may be too high to permit 50-day oscillations to develop.

Oscillations with periods of 20–30 days have been observed near the equator in observations from both the Atlantic (Weisberg and Weingartner 1988) and the Pacific (Legeckis 1977) and in numerical models (Cox 1980; Philander et al. 1986). These oscillations, confined mainly to the mixed layer of the equatorial region between 2°S and 4°N, are seasonally modulated, have wavelengths of about 1000 km, and are westward propagating with an eastward group velocity. Cox (1980) used a multilevel primitive model (Bryan 1969) to study these waves in the Pacific. He found that the energy for the waves was primarily drawn from the mean flow via the horizontal shearing instability between the SEC and the equatorial undercurrent. Baroclinic instability, although of lesser importance, was also found to be a source of perturbation energy. Philander (1986)

using another multilevel model showed that the oscillations derived their energy from the kinetic and potential energy of the mean flow. In both models, instability waves in the upper ocean excite waves that propagate downward (Cox 1980; Philander 1986). These deep waves are primarily Rossby–gravity waves and are also found in the CME model (Böning and Schott 1993).

Several interesting questions arise from these studies and that of Johns et al. (1990). What is the spatial extent of these oscillations? Where is their origin? Is it in the interior of the basin or is it near the western boundary? What is their nature; are they baroclinic Rossby waves as suggested? And finally what are the governing dynamics of the oscillations? To adequately answer these questions, information is required over temporal and spatial scales currently available only from numerical models. Consequently, a lower viscosity CME experiment (N13-2) was chosen in this study to help find answers to these questions. The model is based on the primitive equation model developed at the NOAA Geophysical Fluid Dynamics Laboratory by Byran (1969) and Cox (1984).

The paper is organized in the following manner. The details of the CME simulation and validation studies performed by earlier investigators are found in section 2. Section 3 contains the methodology, which involves model field selection. In section 4 the evolution of the flow fields (section 4a), spectral and wave propagation characteristics (section 4b), and a vorticity analysis (section 4c) are used to describe and determine the nature of the oscillations. A scenario explaining the cause of the oscillations is also developed in this section. In the discussion (section 5) this scenario is discussed in the light of an analytical model (Campos and Olson 1991), while wind forcing and barotropic instability are shown not be responsible for the oscillations. As well, the findings from this study are related to previous studies performed by other investigators and their importance discussed. The summary and conclusions are found in section 6.

2. CME simulation

The numerical simulation used in this paper is the three-dimensional, high-resolution model of the wind-driven and thermohaline circulation of the North Atlantic developed by Bryan and Holland (1989) as the Community Modeling Effort (CME) for the World Ocean Experiment (WOCE). It is based on the primitive equation model developed at the NOAA Geophysical Fluid Dynamics Laboratory by Bryan (1969) and Cox (1984). The primitive equations are solved using a second-order finite-difference scheme on the Arakawa B-grid and conserve total heat content, mass, energy, and tracer variance in the absence of explicit dissipation and forcing (Bryan and Holland 1989). The form of the model equations and the parameterizations developed for this experiment have been summarized by Spall (1990). Further information concerning the model description, the experiment design parameters, and the nomenclature for the various experiments can be found in Bryan et al. (1994). This nomenclature is used throughout this paper.

The model domain extends from 15°S to 65°N, 100°W to 14°E. The horizontal resolution is $1/3°$ in latitude and $2/5°$ in longitude, giving equal grid spacing in the north–south and east–west directions of 37 km at 34°N. This is about equal to the first internal Rossby radius of deformation at midlatitudes; hence the resolution is just adequate to represent many of the eddy processes. There are 30 discrete vertical levels distributed over a maximum depth of 5500 m. The vertical spacing is nonuniform with a minimum of 35 m at the surface and increases to 250 m below 1000 m. Bottom topography is derived from a digital terrain dataset with 5′ latitude–longitude resolution.

Experiment N13-1 was initialized at rest using the January temperature and salinity fields of Levitus (1982) and integrated for 25 years. Surface wind forcing is taken from the monthly mean winds derived by Hellerman and Rosenstein (1983). The surface heat flux is calculated from a bulk formula (Han 1984) as a linear function of the difference between the model-predicted, sea surface temperature, and a prescribed "effective," atmospheric temperature. The timescale of the surface heat flux is on the order of 50 days (Spall 1990) and depends on the latitude, longitude, time of year, and surface temperature. The surface salinity is relaxed toward the Levitus (1982) climatology also with a timescale of 50 days. Linear interpolation between monthly and seasonal means is used to obtain necessary values for all surface forcing fields at each model time step. Snapshots of the model fields were saved every three days.

Experiments N13-1 and N13-2 were calculated using different values for the coefficients of vertical and horizontal diffusion. Fields from N13-1 (start of year 20) were used as initial conditions for N13-2, which was run for five more years. In N13-1, lateral friction was represented by a biharmonic operator with a coefficient of -2.5×10^{11} m^4 s^{-1} for both momentum and tracers. The vertical dissipation mechanism is a second-order operator with constant coefficients of 3.0×10^{-3} m^2 s^{-1} for momentum and 3.0×10^{-5} m^2 s^{-1} for tracers. In N13-2, the biharmonic friction was reduced by a factor of 2.5 and vertical momentum mixing was reduced by a factor of 3. Additional dissipation of momentum was provided in both cases by a quadratic bottom drag. A Kraus–Turner (1967) type surface mixed layer was included at the top of the model. It was found to be largely unimportant as it did not penetrate beyond the top layer of the model (F. Byran 1994, personal communication). A conventional adjustment scheme was used to treat free convective mixing (Bryan and Holland 1989).

Validation studies performed on the output from several different CME calculations (Bryan and Holland 1989; Schott and Böning 1991; Didden and Schott 1992) showed that the main features and seasonality of the tropical surface currents, as revealed by observational studies (Richardson and McKee 1984; Richardson and Reverdin 1987), were reproduced in each case. During the fall, the CME versions show the NBC flowing northward along the coast of South America until it retroflects around 7°N to form the western arm of the eastward flowing NECC. During spring, westward flow has replaced the NECC and the NBC flows northwestward along the South American coast.

Schott and Böning (1991) considered fields from a CME version where the vertical diffusion coefficient was a factor of 3 less than that used in N13-1 (same value as used in N13-2). The velocity fields in this case were found to be more realistic in the equatorial region than those from N13-1. In particular, the Equatorial Undercurrent (EUC) did not penetrate far enough eastward in N13-1; its core speed was only 0.3 m s^{-1} at 30°W in February. Speeds of greater than 0.60 m s^{-1} have been reported in the real EUC core at 1°E in February (Hénin et al. 1986). In the less viscous solution the core speeds were 0.90 m s^{-1} at 30°W, suggesting that this solution better represents the equatorial circulation. The EUC, however, surfaced persistently in the west during winter. Surfacing of the EUC has been observed occasionally in the real ocean (Katz et al. 1981). In the northern Tropics, the NECC displayed two cores: a narrow meandering jet on the southern edge of the NECC (3°N) and a wider core at about 6°N. Meandering of the NECC has been reported by Richardson and Reverdin (1987); however, the penetration of the jet far into the interior is unrealistic. Two separate NECC cores have occasionally been observed in the real ocean (Hénin and Hisard 1987).

Didden and Schott (1992), using the same CME version as that of Böning and Schott (1991), compared the seasonal cycles of sea surface height (SSH) and geostrophic surface currents from two years of Geosat altimetry and one year of model output in this region. They found that the large-scale structure of the annual harmonic SSH variability, consisting of two bands of maximum variability, centered at about 3° and 12°N, with a relative minimum along 7°, was similar in both products. In these regions, more than 60% of the total variance is explained by the annual harmonic variance. The annual harmonic of geostrophic velocity also showed good agreement. In both cases a band of strong zonal flow anomaly, which is westward (eastward) in April (October), is seen between 4° and 6°N, 35° and 45°W. The pronounced meander pattern of the model NECC was not found in the altimeter annual harmonic velocities. Meridional profiles of zonal velocity anomalies were calculated from both sources to show principal features of the region. In both sets of fields, the two NECC cores are seen together with the seasonal meridional migration of the southern core.

Since the fields from the western Tropics were required for this study, the CME calculation producing the most realistic fields in this region was chosen for use in this paper. The findings of Schott and Böning (1991) and Didden and Schott (1992) suggest that N13-2, whose vertical diffusion coefficient has the same value as that of Schott and Böning (1991), is the most appropriate choice for this study. Neither the surfacing of the EUC nor the eastward penetration of the NECC jet will impact upon this study, as the 50-day oscillations discussed in the following sections are not found near these features.

3. Methods

a. Model field selection

To carry out this study, it was necessary to extract the subset of the N13-2 solution that was likely to contain the signature of the 50-day oscillations. The following choices were made to ensure that the oscillation signal was adequately represented in the extracted fields as well as facilitating easier management of the model output. The tropical region of the model extending from 5°S to 15°N, 60°W to 5°E was chosen as the domain of the extracted fields. The last 256 three-daily snapshots of the N13-2 solution were retrieved to ensure that several oscillation cycles were resolved. These snapshots served as the population underlying the statistical analyses discussed in the following section. The time interval between each model realization is three days; hence, a little over two years (779 days) of the solution was extracted. The grid was subsampled in the longitudinal direction, producing a spacing of 1.2° (about 120 km). The latitudinal spacing is that of the model solution (1/3°). Stammer and Böning (1992) calculated zonally averaged characteristic eddy length scales in N13-1, obtaining a value of about 120 km at 10°N. Sensitivity studies showed that decreasing model friction decreased this estimate. The zonal wavelength of the observed 50-day oscillations is 520 km with a range of 390–740 km; hence the model is capable of resolving these structures. In addition, it was noted that the signature of 50-day oscillations is strongest in the surface waters; hence the top eight levels (upper 400 km) of the N13-2 solution were extracted. The variables obtained were temperature, salinity, zonal and meridional velocity, and vertical velocity. This subset will be known as N13-2E in the following discussion.

To capture the oscillation throughout the surface waters, the zonal and meridional velocities were depth averaged over the surface layer of N13-2E. For the purposes of this study, the surface layer is defined as the layer between the 23°C isotherm and the free surface. Boyd (1986) categorized the flow in the upper kilometer of the water column in the western tropical At-

lantic into four regions. Using mean temperature and salinity (T–S) curves for this area (Emery and Dewar 1982), she chose the surface layer to lie between the 23° and 27°C isotherms, which corresponds, in the western basin, to water depths between 0 and 80 m. The N13-2 T–S relationships in this region will shortly be shown to be similar to those obtained by Emery and Dewar (1982); hence it is reasonable to define the N13-2E surface layer in the same manner. In N13-2E, the mean position of the 23°C isotherm shoals toward the east; it is found at about 110 m at 50°W and 80 m at 35°W. Hence, three vertical grid points were used when depth averaging in the western basin and two points in the interior. All velocity fields discussed below are depth averaged unless otherwise stated.

Emery and Dewar (1982) computed annual mean T–S relationships for 5° squares in the Atlantic Ocean. To facilitate a comparison between the model and observations, temperature and salinity model fields were temporally averaged to produce an annual mean for a region delimited by one of the squares used by Emery and Dewar (1982) in the western Tropics. Figure 1 shows their T–S relationship for the region west of 40°W between 5° and 15°N and that for N13-2. The latter relationship was obtained by first temporally averaging the ten temperature and salinity fields comprising each month of the five years of the simulation. These 50 monthly values were then averaged to produce an annual mean. These temporal averages were then extracted between Brazil and 40°W along 7.5°N. Since all T–S points were plotted, an envelope of values can be seen in the deeper layers. The two relationships generally agree, although the N13-2 upper water is slightly cooler and fresher than the observed upper layer T–S points. The two sets of values converge again at the surface, which is to be expected since the model surface salinity is restored to the Levitus climatological values.

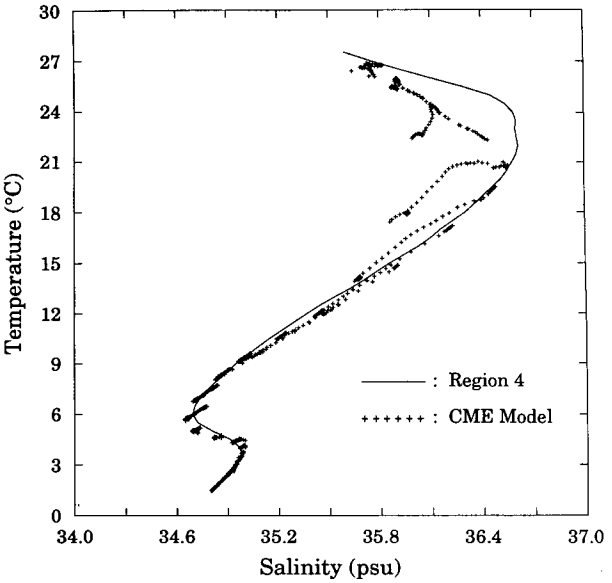

FIG. 1. Annual mean potential temperature–salinity relationships from Region 4 (west of 40°W between 5° and 15°N) from Emery and Dewar (1982) and from 7.5°N between Brazil and 40°W in N13-2.

4. Results

a. Description of model flow fields

A sequence of velocity component snapshots, selected at monthly intervals over an annual cycle from the western tropical region of N13-2E, were examined to follow the evolution and decay of major flow features. The onset and decay of the retroflection and the NECC is reflected in the zonal velocity contours. The meander pattern associated with the NECC during the retroflection is seen in the meridional velocity contours. As well, wavelike structures are seen in these contour fields once the NECC has slowed and disappeared. These waves will later be shown to be 50-day oscillations. Five snapshots that are representative of particular stages of the evolution and decay of the flow are shown and discussed below. The flow patterns in the remaining months are extremely similar and are, therefore, discussed but not shown.

The sequence consisted of snapshots from the middle of each month starting in July of the second last year of the CME simulation (year 23) and finishing in the following July. Two cores of eastward flow associated with the NECC are seen in July (Fig. 2a): the jet to the south and the broader slower flow to the north. The westward flow of the NEC and the northern branch of the SEC are seen to the north and south of the NECC. Alternating bands of northward and southward flow are seen in the meridional velocity contours (Fig. 2b) in the region of the standing meander pattern of the NECC jet. This pattern is repeated in August (Figs. 3a,b) and September; however, the eastward flow in the NECC jet and the meridional flow associated with the meanders intensified. The meanders have penetrated farther eastward between July and August. In October and November, the flow magnitudes decrease slightly in these key regions; however, the patterns are largely unchanged. Pockets of westward flow appear north of the NECC jet in both months.

In January, westward flow is seen across the entire basin north of the NECC jet, which has slowed considerably (Fig. 4a). Similar behavior was seen in the December snapshot. The alternating bands of northward and southward flow of the meander pattern in January have translated westward (Fig. 4b), whereas earlier these bands were stationary. By the middle of the next month, February, the eastward and westward flows are of about the same magnitude and westward flow has infiltrated most of the basin. Remnants of the eastward NECC remain (Fig. 5a). The alternating bands seen in the meridional velocity contours are more pronounced

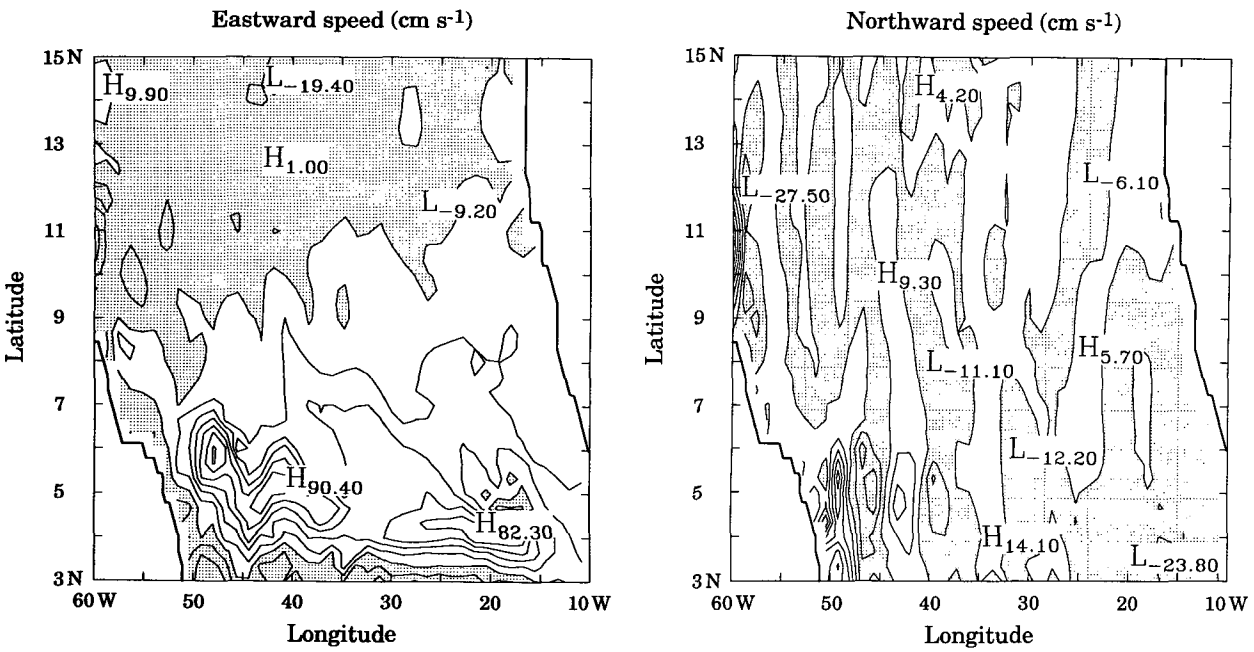

FIG. 2. Contours of surface layer (a) zonal and (b) meridional velocity from mid-July in model year 23. Contour interval is 15 cm s^{-1} and the hatched regions represent westward and southward flow.

in the west and are weakening in magnitude in the interior (35°W) (Fig. 5b). The zonal component of flow behaves similarly in March and April, while alternating bands of meridional flow are found to be weakening in the west and disappearing entirely in the interior. By May, the alternating bands are no longer observed (Fig. 6b) and the flow is predominantly westward (Fig. 6a). In June, the NECC is seen to start up again and alternating bands of northward and southward flow are seen in the western basin. By July, these meanders have pen-

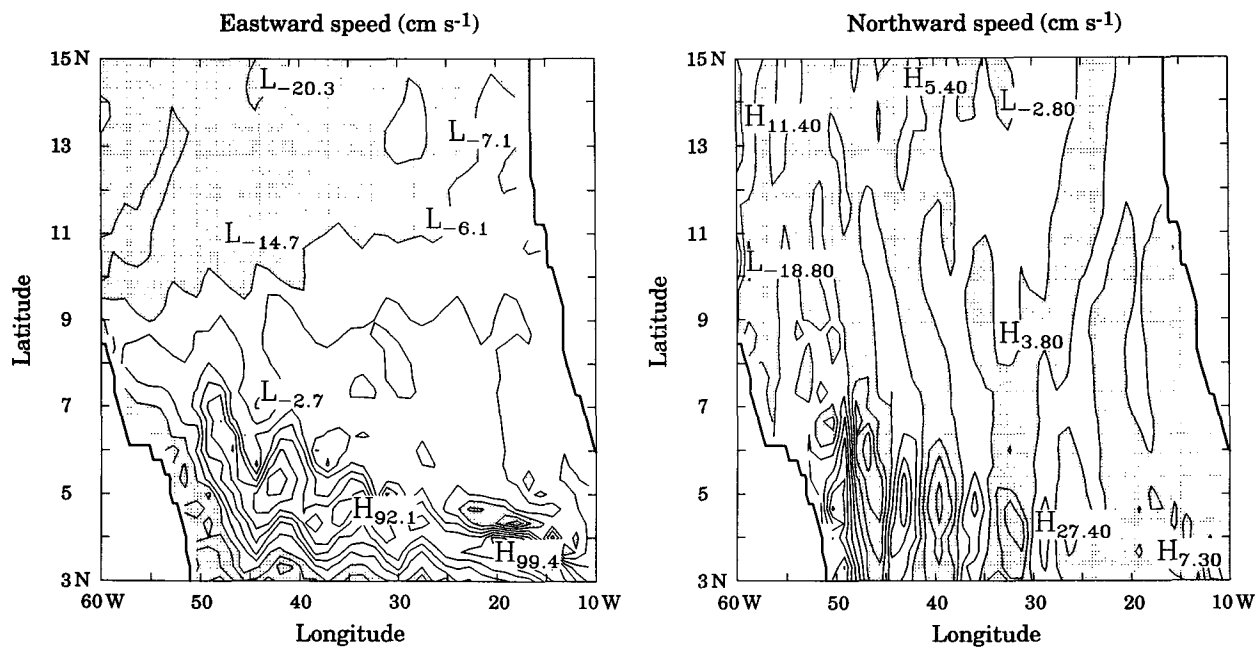

FIG. 3. Same as Fig. 2 but for mid-August of model year 23.

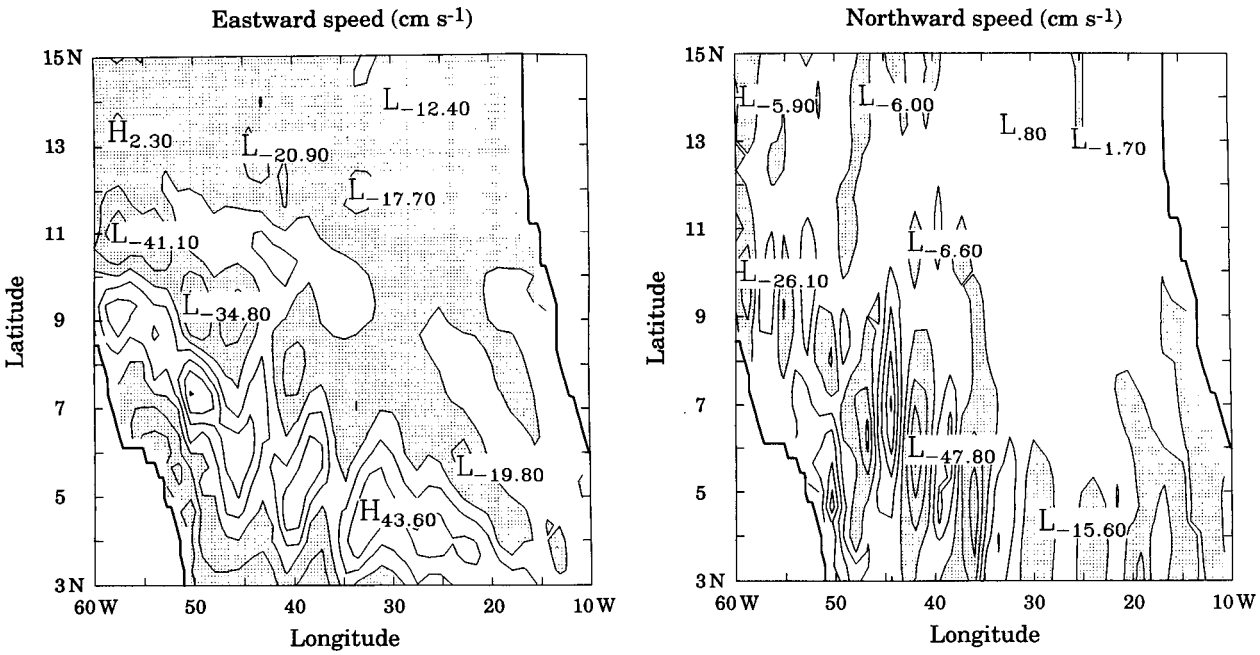

FIG. 4. Same as Fig. 2 but for mid-January of model year 24.

etrated into the interior (35°) and the NECC has intensified again.

This time history of the flow in the western Tropics suggests that the meander pattern, represented by wavelike structures in the meridional velocity snapshots, is held stationary by the NECC during the retroflection period and then moves westward as the NECC weakens. It is also possible, however, that these displacements are due to simple temporal changes. The structures in the meridional flow weaken with time and disappear first in the interior of the basin and finally disappear altogether before the retroflection starts up

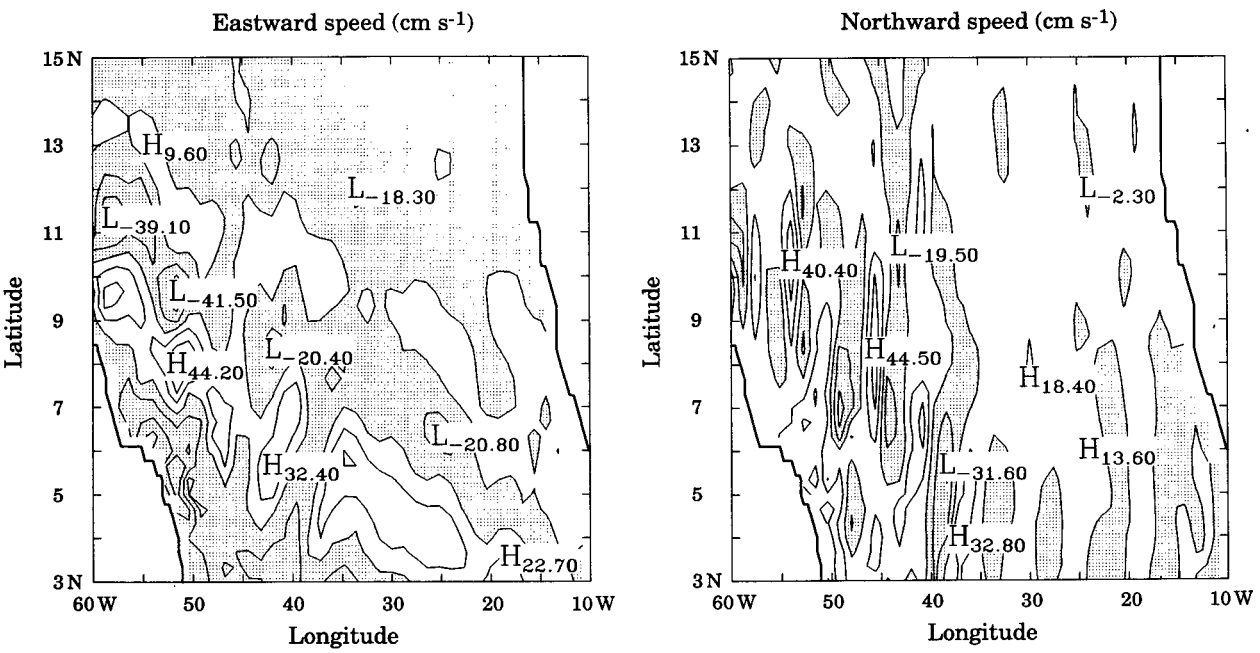

FIG. 5. Same as Fig. 2 but for mid-February of model year 24.

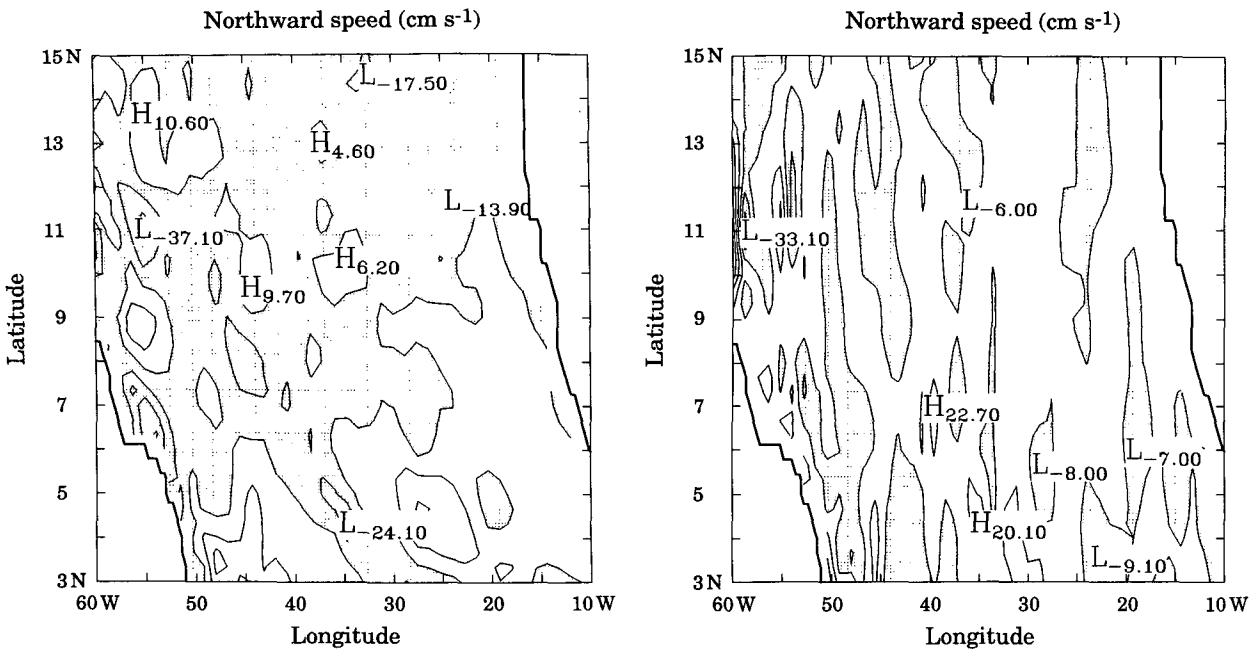

FIG. 6. Same as Fig. 2 but for mid-May of model year 24.

again. It will be shown in the remainder of this section that oscillations of the meridional component of velocity, with periods of 50 days, occur in this region at fixed locations from December through April. As well, they will be shown to be advected westward along the same path as the wavelike structures discussed here.

b. Spectral and wave propagation characteristics

The first step in these analyses was to establish that a significant signal occurred in the meridional velocity component at or near 50 days. To do this the variance of the meridional component (V) of velocity in the 40–60-day band was calculated (Fig. 7). This band was chosen by Johns et al. (1990) when investigating 50-day oscillations; hence it is used here. Energy is seen in the western region of the domain between 3° and 13°N, 60° and 30°W. Three regions of "high" variance are seen. At 5°N, 36°W and 11°N, 55°W the variance exceeds 50 cm^2 s^{-2}, while at 7°N, 50°W it is greater than 150 cm^2 s^{-2}. To check that this variance is primarily from the 50-day signal, the calculation was repeated using the 50–55 day band. The same spatial distribution of energy is seen for the 50–55 day band (not shown); however, the magnitudes are somewhat reduced: at 5°N, 36°W and 11°N, 55°W the variance is about 40 cm^2 s^{-2} and at 7.5°N, 50°W it exceeds 120 cm^2 s^{-2}. Hence, there is a small contribution from energy in the 40–50 day band; however, this signal is most likely due to doppler shifting of the 50-day oscillations by mean currents and will be discussed shortly. Hence, it is appropriate to use the 40–60 day band in the following analyses.

Time series of the 40–60 day bandpassed filtered meridional velocity at these three locations are seen in Fig. 8. The start of the time series corresponds to day 316 (November) of the third last year of the N13-2 simulation (model year 22); hence the time axis has been offset by −49 days so that the last two years of the series can be read easily in Julian days. Two sets of wave packets are seen in each of the time series. Since the amplitude and duration of the packets at a particular location are quite similar to each other from year to year, only the details of the second wave packet will be discussed here. At 5°N, 36°W the onset of this packet occurs in November at about Julian day 324 of the time series. The start of the first cycle in the wave

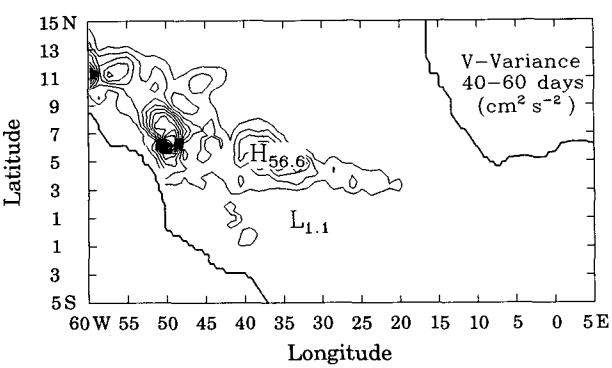

FIG. 7. Variance of the surface layer meridional component of velocity (in cm^2 s^{-2}) between 40 and 60 days. Contour interval is 10 cm^2 s^{-2}.

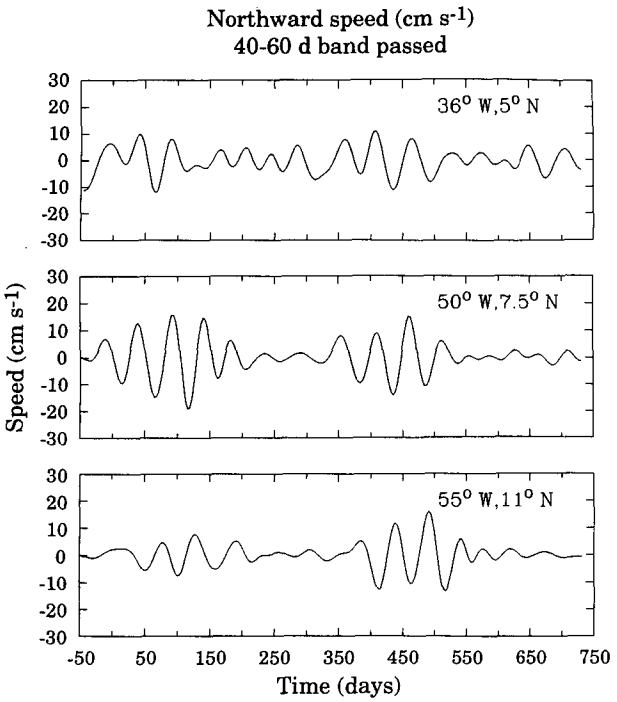

FIG. 8. Time series of bandpass filtered (40–60 days) surface layer meridional velocity (cm s^{-1}) at 5°N, 36°W; 7.5°N, 50°W; and 11°N, 55°W. The time series starts at day 316 (November) of model year 22 and finishes at the end of year 24. The time axis has been offset by −49 days, so that the last two years can be read in Julian days.

packet is identified by a wave trough. The cycles in the wave packet have periods of about 52 days. Roughly 60 days later, a wave packet is seen at 7.5°N, 50°W; the period of its waves is about 52 days. A similar packet appears 30 days later at 11°N, 55°W. These lags in the appearance of the wave packet at progressively westward locations suggest that the packet is either propagating or being advected westward. If the former case is true, the group speed of the packet is 0.2–0.3 m s^{-1}. The wave packet at 5°N, 36°W contains three cycles (about 170 days) and is seen to have decayed by May (around day 487 of the time series). Evidently these oscillations are seen to appear at the end of the retroflection period and disappear just prior to it starting up again. Some evidence of wave packets are seen in the time series of zonal velocity, bandpassed filtered between 40 and 60 days, at the three locations discussed above (not shown). The packets are not as evident as those in the meridional component of velocity. The amplitudes are somewhat less than half those of the amplitudes of the bandpassed filtered meridional velocities.

Variance-preserving spectra of meridional velocity were then calculated at the high variance locations. At 7.5°N, 50°W a peak of about 230 cm^2 s^{-2} is seen to be centered at 52 days (Fig. 9b). Energy in other bands is seen to be an order of magnitude smaller. The main peak at 11°N, 55°W (Fig. 9c) occurs near 70 days, while the spectral value at 52 days is 40 cm^2 s^{-2}. At 5°N, 36°W (Fig. 9a) the largest peak occurs at 86 days and has a value of about 440 cm^2 s^{-2}. Another smaller peak (140 cm^2 s^{-2}) occurs at 52 days. The peak at 86 days may be due to the inadequate resolution of the 100-day period; two years of data may not be enough to resolve this signal properly. These spectral analyses confirm that a significant signal at or near 50 days is present in the meridional component of velocity at these locations, in particular at 50°W.

A longitude–time plot of 40–60 day bandpassed filtered meridional velocity was constructed along 6°N from 60°W to 10°W (Fig. 10). The time series as noted earlier, begins about 1 1/2 months before the start of model year 23 (month 0) and finishes at the end of model year 24. The plot is dominated by two wave packets with eastward group velocity and westward phase speed. The first is seen between December of year 22 (month 1) and April of year 23 (month 6), while the second starts up in mid-December (month 13). The westward phase speed is around 0.12 m s^{-1}, while the eastward group velocity is about 0.09 m s^{-1}, which conflicts with the westward group velocity inferred from Fig. 8. The wavelength of the oscillations is about 600 km in the interior, shortening to about 500 km near the western boundary. Their period is nearly 2 months. They disappear around May (month 18) of year 23.

The snapshots of velocity for mid-July and mid-August, discussed above, showed the intensification of the NECC and the eastward movement of the associated meanders. In the longitude–time plot a wave signal is generated at 50°W in mid-July of year 23 (month 9). The appearance of this signal coincides with the start-up of the retroflection period and the buildup of the strength of the eastward NECC jet (Figs. 2a,b). A time–longitude plot of the total meridional velocity (not shown) shows a standing wave pattern between 52° and 35°W from August to December. Hence, it is most likely that the signal generated at the western boundary is advected eastward by the NECC during its intensification phase. Once the NECC has set up, the eastward flow balances the westward phase velocity of the signal, producing a stationary wave. This is maintained until the NECC starts to weaken (December) when individual wave crests are released to propagate westward. The eastward group velocity, however, is in conflict with the results from Fig. 8, which implied that the wave packets were moving westward. This apparent discrepancy may be explained by westward advection. Since the eastward group velocity is small, it could be overridden by westward advection. Substantiating evidence for this idea will be presented later in this section.

Preliminary identification of these oscillations is possible by considering the dispersion relation for plane, off-equatorial baroclinic Rossby waves. It

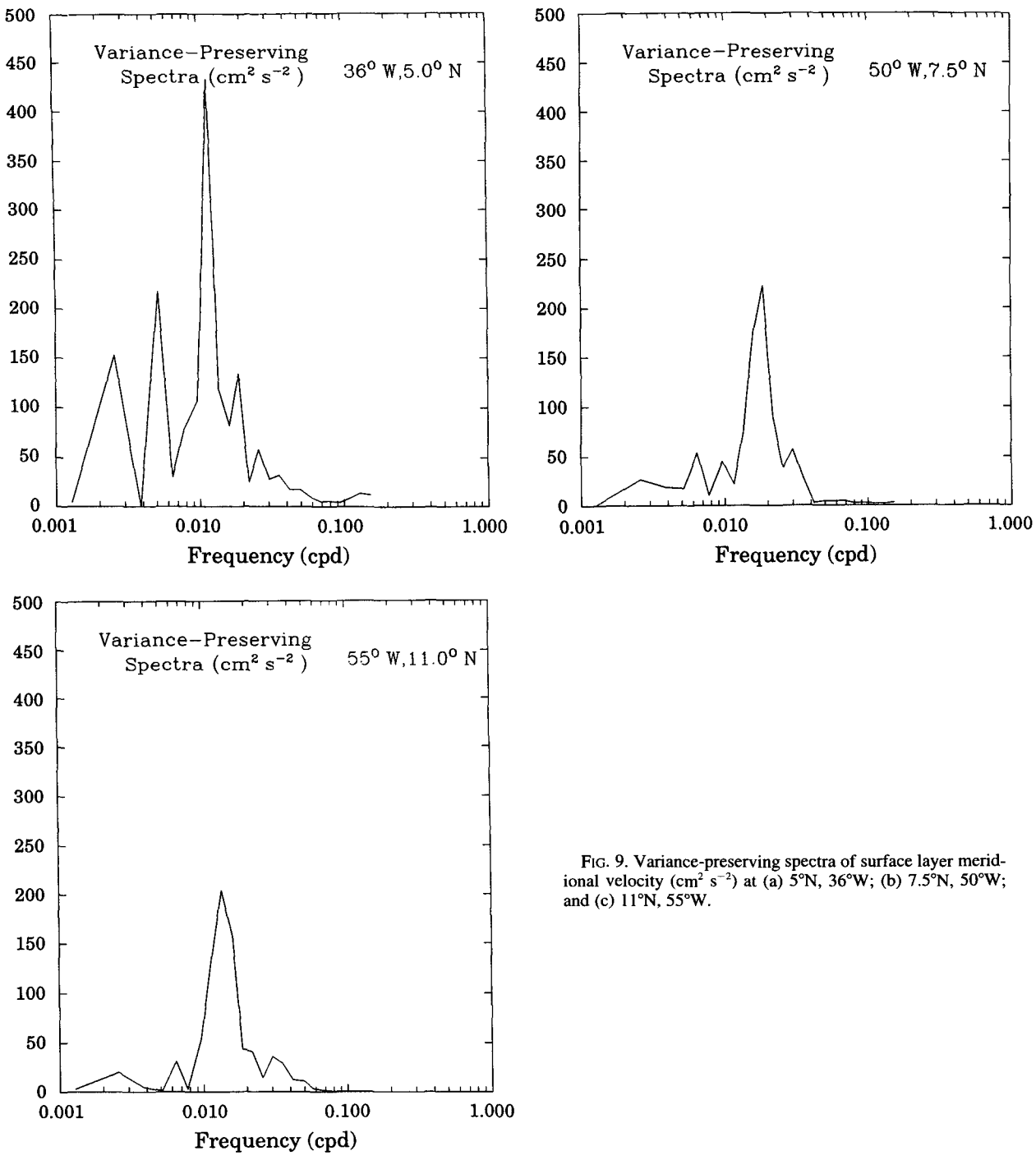

FIG. 9. Variance-preserving spectra of surface layer meridional velocity ($cm^2\ s^{-2}$) at (a) 5°N, 36°W; (b) 7.5°N, 50°W; and (c) 11°N, 55°W.

should be noted that the use of linear theory is not strictly correct here since the phase speed of the oscillations and the anomaly velocities are roughly the same size (around 0.1 $m\ s^{-1}$), suggesting that nonlinear terms are affecting the linear solution over the period of the wave (Gill 1982). Linear tools, however, provide a good starting point when trying to understand these oscillations. Also, when nonlinear contributions are important they cause the spectrum to evolve and the observed wave form or spectrum does not persist (Gill 1982). In this study the anomalies are seen to persist in the same form for 4 to 5 months. Such persistence implies that nonlinear effects are not dominating the solution; hence linear

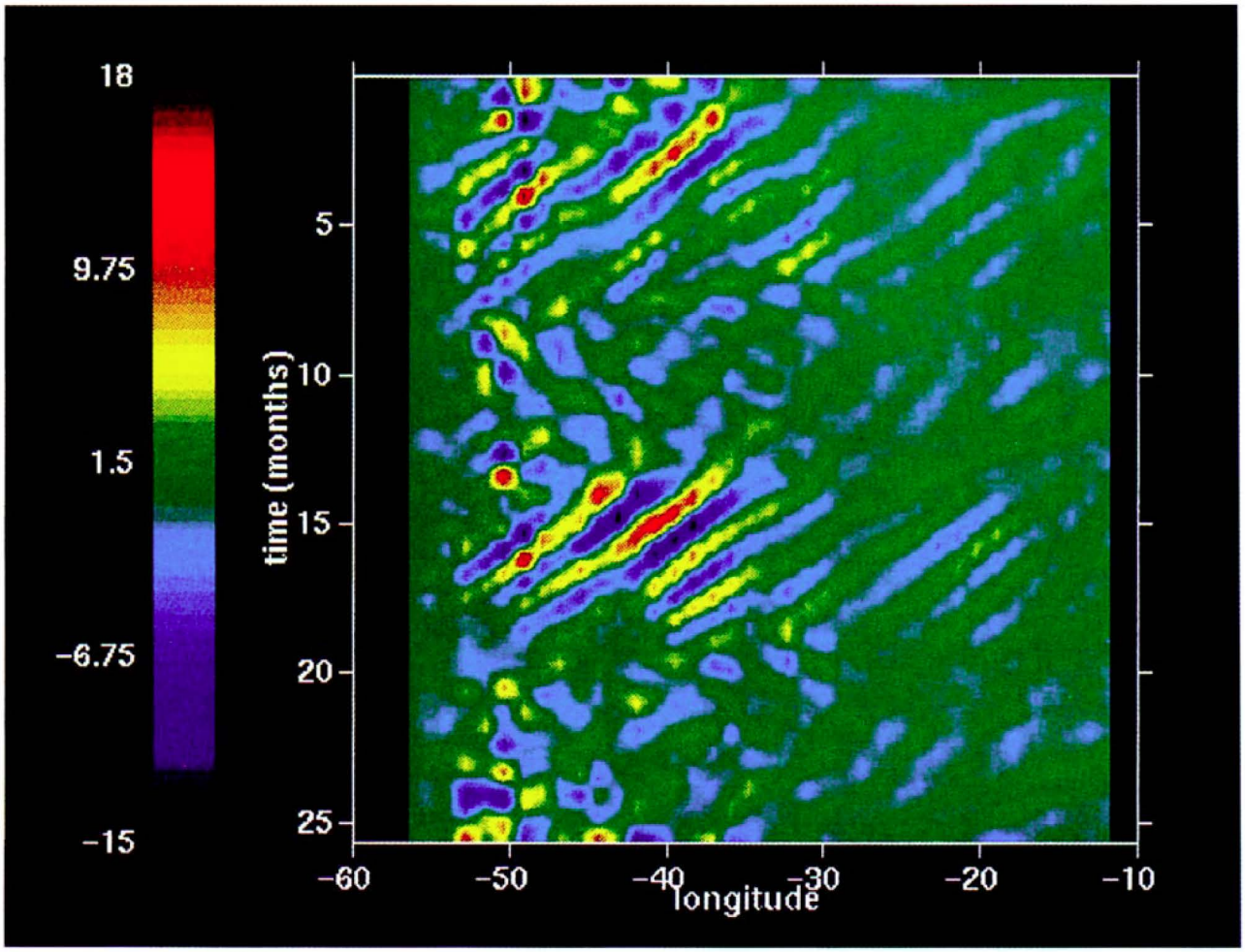

FIG. 10. Longitude–time plot of the 40–60 day bandpass filtered surface layer meridional velocity (cm s^{-1}), along 6°N from day 316 (November) of model year 22 to the end of model year 24.

analysis tools, although not entirely describing the waves, provide some understanding of their nature.

The dispersion relationship is

$$\omega = \frac{-\beta k}{k^2 + l^2 + R_n^{-2}},$$

where ω is the wave frequency, β the planetary vorticity gradient, k and l are the zonal and meridional wavenumbers, and R_n the internal Rossby radius of deformation for the nth baroclinic mode (Pedlosky 1987). The off-equatorial relationship can be used since these oscillations are seen more than one equatorial Rossby radius from the equator (Gill 1982). This value is roughly 400 km (Emery et al. 1984) and the oscillations are not found south of 5°N (550 km from the equator). The first baroclinic deformation radius R_1 for this region from the model is about 115 km. The wavelength of the filtered oscillations in the longitude–time plot is about 600 km. The associated wavenumber k is -1.05×10^{-5} m^{-1}; l is assumed to be zero since the direction of propagation of the signal as shown by the V variance (Fig. 7) is almost zonal. The phase speed and the period calculated for the Rossby wave relationships are -0.12 m s^{-1} and 56 days. These values compare well with the inferred values of the zonal phase speed and period.

In the case of a Rossby wave, the group velocity is directed eastward when $k^2 > R^{-2}$, which is occurring here. The theoretical Rossby wave group velocity formulation in the x direction, C_{gx}, calculated using these k and R values, gives a value of 0.02 m s^{-1}. This value is slower than that obtained from the time–longitude plot (0.09 m s^{-1}). The difference is most likely due to nonlinear effects and the accuracy of the diagram. As noted, this result conflicts with the westward packet propagation inferred from the meridional time series in Fig. 8. These packets were seen after the breakdown on the NECC, so they occur during the time when

westward flow is setting up in the region. A possible explanation of these conflicting findings is that since the group velocity is small, it is being overridden by westward advection. Schott and Böning (1991) documented disorganized but generally westward flow during February north of 2°N in the top model layer. The disorganized flow is probably due to the wave/eddy effects. To determine if westward flow was present from February through April and to smooth the chaotic effects reported by Schott and Böning (1991), the flow field from the top layer was averaged over this period (Fig. 11). The resulting field shows flow with largely westward components in the region through which the oscillations are moving (5°N, 36°W and 7°N, 50°W). Hence, westward advection of the wave packets quite likely explains this discrepancy.

Linear theory has provided a means of establishing the nature of these waves as baroclinic Rossby waves. Discrepancies arise due to nonlinear interactions, especially the interaction of mean currents and the oscillations. Another nonlinear effect is doppler shifting. The mean westward flow in the region through which the waves move and for the period they are seen is 0.04 m s^{-1}. Doppler shifting of 50-day oscillations by this current would result in an observed frequency of about 40 days. Since the band passing was performed between 40 and 60 days, the doppler shifted signal will be included in the above analysis.

A comparison of the results from these analyses and those obtained by Johns et al. (1990) revealed some similarities. The oscillations in both cases exhibited a mean periodicity of about 50 days. In the CME model, the oscillations were only seen from December through April, while in the observations they were seen throughout the year. The period, however, varied in the observations from 40 days in spring to 60 days in fall. Significant energy was found in both cases at periods of about 50 days, and the phase speeds and wavelengths were about the same magnitude. In both cases, the waves were considered to approximate first-mode baroclinic Rossby waves, with the caveat that the group speed of the model oscillations appears to be in the wrong direction. However, this discrepancy may be explained by westward advection. Also, it should be noted that the observed oscillations were documented over the continental slope, while those in the model were found over most of the western Tropics.

c. *Vorticity analysis of 50-day oscillations*

It would appear from the time history of the depth-averaged velocity fields discussed earlier, that a meander pattern expands eastward as the NECC develops and retreats westward as the NECC weakens and vanishes. These meanders weaken with time and disappear first in the interior of the basin and finally disappear altogether before the retroflection starts up again. They move westward along the same path and at the same time as the 50-day oscillations discussed above; hence it is reasonable to consider the oscillations and the meanders to be the same phenomenon. To verify the dynamics suggested by the time history and further validate the claim that the 50-day oscillations are indeed Rossby waves, a vorticity analysis was performed on snapshots of velocity taken from the retroflection and nonretroflection periods. These analyses are based on all available grid points in the study region, not the N13-2E subset.

The first snapshot discussed is from February when the 50-day oscillations are most pronounced and the

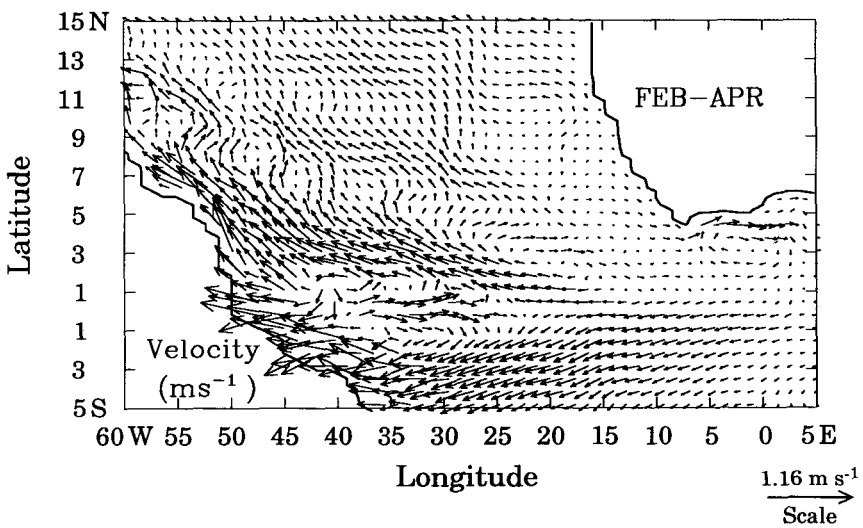

FIG. 11. Temporally averaged velocity fields (m s^{-1}) for the period February–April of model year 24 from model level 1 (17.5 m).

retroflection is absent. The leading balance obtained is that known to represent Rossby waves. The dominant modes of these waves were then identified from a modal decomposition and the vorticity analysis was repeated using the flow fields associated with the barotropic and first three baroclinic modes. The vorticity analysis was then performed using an undecomposed snapshot from the retroflection period, since modes can no longer be separated in the presence of a mean current such as the NECC. The same leading balance was obtained; hence the meanders are also Rossby waves in an eastward zonal current. Consequently, one can say that the 50-day oscillations are the residue of the meander pattern associated with the NECC.

In this study, the vorticity analysis scheme developed as part of the PRE-EVA (Primitive Equation Energy and Vorticity Analysis) package (Spall 1989) was used to obtain the leading balance in the full vorticity analysis equation. It is derived from the energy and vorticity (EVA) scheme developed and used by Pinardi and Robinson (1986, 1987). The package calculates all the terms in the full vorticity equation from the output of a primitive equation model. The version used in this thesis was specifically formulated by Spall for the CME model (Spall 1992). The equation for the time rate of change of the vertical component of relative vorticity was obtained from the horizontal momentum equations by cross-differentiating the momentum equations and summing to eliminate the pressure. The resulting equation is

$$\zeta_t = -\mathbf{u}_H\cdot\nabla\zeta - \beta v + fw_z + \zeta w_z - w\zeta_z - (u_z w_y - v_z w_x) + B\zeta_{zz} + F_h + T.$$

Each of the terms are explained in Table 1. The truncation error warrants special attention; it is due to the misrepresentation of spatial derivatives in the vorticity equation that arises when finite-difference schemes are used. The package solves the vorticity equation term by term and then calculates the time rate of change of relative vorticity ζ_t as a residual. The package creates horizontal maps of each of the terms over some specified region at a particular model level.

The first snapshot of velocity subjected to the vorticity analysis was taken from the start of February (field D033.48) in the last year of N13-2, the time at which 50-day oscillations are known to be most pronounced. The analysis must be performed at a particular level; the middle of the third layer (92 m) was chosen in this case. This depth was selected as it lies largely outside of the influence of the surface boundary conditions. Since the surface salinity is relaxed back to Levitus (1982) climatology, instabilities associated with convective overturning may occur. The effects of these instabilities are unlikely to penetrate farther than the top two layers of the model. Also, the modal decomposition (to be discussed shortly) revealed that the zero crossings for the first and second baroclinic modes were well below this depth; consequently, the wave signal is detectable in these velocities.

TABLE 1. Explanation of terms in the vorticity equation.

Vorticity equation terms	Explanation
ζ	Relative vorticity
ζ_t	Time rate of change of relative vorticity
$\mathbf{u}_H\cdot\nabla\zeta$	Horizontal advection of relative vorticity
β_v	Horizontal advection of planetary vorticity
fw_z	Stretching of planetary vorticity
ζw_z	Stretching of relative vorticity
$w\zeta_z$	Vertical advection of relative vorticity
$u_z w_y - v_z w_x$	Vorticity by twisting of horizontal velocity fields
$B\zeta_{zz}$	Vertical diffusion of relative vorticity
F_h	Horizontal diffusion of relative vorticity
T	Truncation error, nonconservative term

The analysis yielded horizontal maps of the terms in the vorticity equation over the area of interest. Balances in the western boundary layer are likely to be more complicated than in the interior and a clear understanding of the nature of the oscillations may not be obtainable there. Consequently, the region of interest was limited to the interior (5°–11°N, 48°–31°W). In the region through which the waves are known to propagate (5°N, 35°W to 7°N, 48°W), the leading terms are the horizontal advection of relative vorticity and planetary vorticity (Figs. 12a,b), stretching of planetary vorticity (Fig. 12c) and the time rate of change of relative vorticity (Fig. 12d). Alternating bands of highs and lows are seen in each of these terms, although this pattern is less coherent in the stretching term. The terms are mostly in phase. There is a contribution from the twisting term (not shown) in isolated patches but it does not display the same spatial distribution as the other leading terms. The remaining terms are an order of magnitude smaller than those already discussed. Outside of the oscillation region, no significant contribution is made by any of the terms. It appears that the balance in this case is

$$\zeta_t = -\mathbf{u}_H\cdot\nabla\zeta - \beta v + fw_z.$$

This balance, as mentioned earlier, is the vorticity balance for advected baroclinic Rossby waves. It should be noted, however, that the magnitude of the $\mathbf{u}_H\cdot\nabla\zeta$ term is larger than the other two terms. This advection term will be dominated by $u\partial\zeta/\partial x$, since there is no significant mean component of flow in the meridional direction at this time (Fig. 5b). The "path" along which the oscillations move (Fig. 5b) lies in a region of westward flow (Fig. 5a); hence the vorticity field is most likely being advected westward. The next most important term is βv and there is some contribution from fw_z.

Prior to performing the decomposition, the time rate of change of relative vorticity, ζ_t, was determined independently to check the validity of calculating this

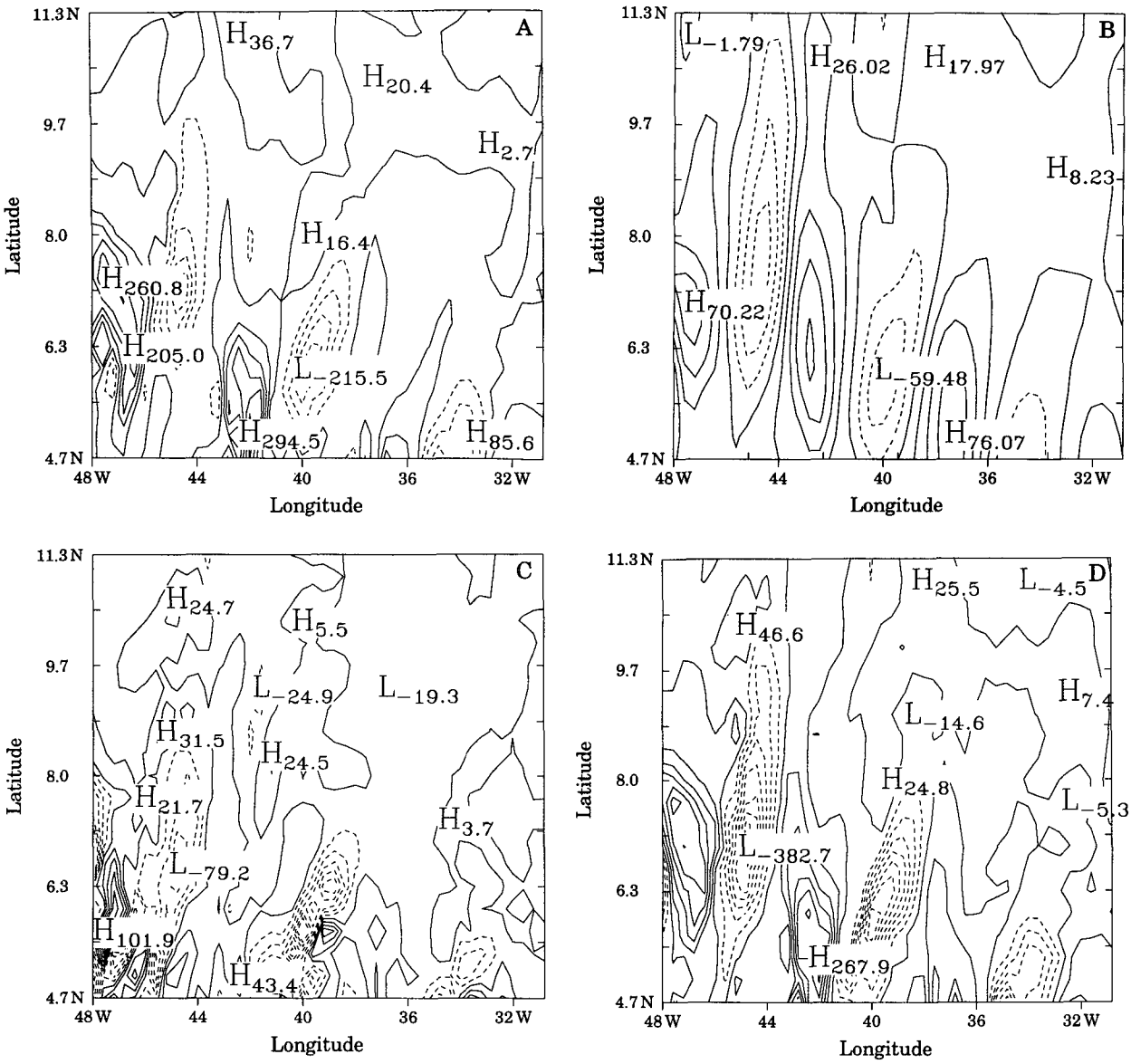

FIG. 12. Leading balance of terms from full vorticity equation: (a) horizontal advection of relative vorticity, $\mathbf{u}_H \cdot \nabla\zeta$ ($\times 10^{-13}$ s^{-2}); (b) horizontal advection of planetary vorticity, βv ($\times 10^{-13}$ s^{-2}); (c) stretching of planetary vorticity, fw_z ($\times 10^{-13}$ s^{-2}); and (d) time rate of change of relative vorticity, ζ_t ($\times 10^{-13}$ s^{-2}) for February (D033.48) at 92 m.

term as the residual of the full vorticity equation. Fields of relative vorticity ζ were also produced by this package; hence ζ_t can be obtained by calculating ζ at two successive times separated by about three days (D033.48 and D036.5). The resulting ζ_t field (Fig. 13) displayed similar patterns to that calculated as a residual (Fig. 12d); however, the magnitudes were smaller. This discrepancy can be explained by the three-day time interval used in the finite-difference scheme. This interval represents how often model fields are stored and is much greater than the model time step. If the ζ fields had been more closely spaced together in time, the magnitudes would have been similar. It appears that calculating ζ_t as a residual produces a reasonable result.

It is apparent that the fields are noisy. At some particular location (5°N, 45°W), the magnitudes of the terms balance while at others the balance is not as exact. To remove some of the noise in these fields, as well as identify the dominant wave modes, a modal decomposition was performed. The decomposition acts to "filter out" unwanted signals not associated with that of the waves.

The analyses in the previous section suggested that the oscillations were first-mode baroclinic Rossby

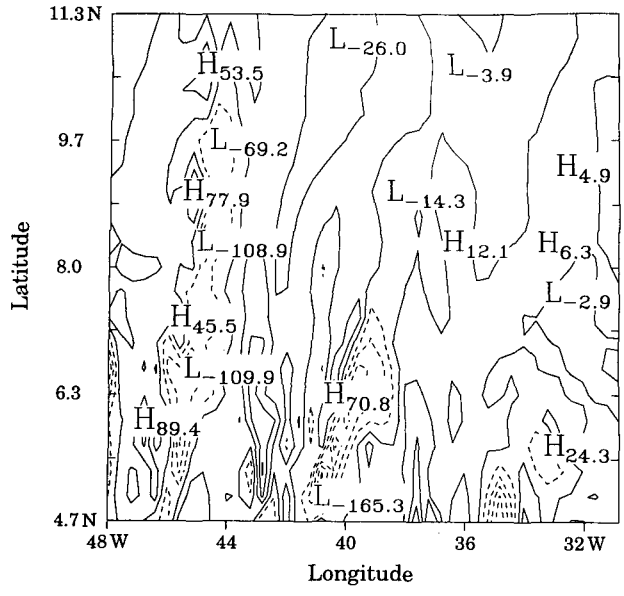

FIG. 13. Time rate of change of relative vorticity ($\times 10^{-9}$ s^{-2}) calculated at two successive times separated by about three days (D033.48 and D036.52).

waves. To determine if this is so, a normal-mode decomposition was performed on the horizontal velocity fields. The vertical velocity eigenfunctions $\hat{w}_n$ and eigenvalues c_n were found by solving the following equation numerically with a rigid lid and a constant depth ocean, H:

$$d^2\hat{w}_n/dz^2 + (N^2/c_n^2)\hat{w}_n = 0$$

$$\hat{w} = 0 \quad \text{at} \quad z = 0, -H,$$

where N is the Brunt–Väisälä frequency. The $N^2(z)$ profile used in the equation was created by first averaging the vertical profiles of temperature and salinity over the region that was used in the vorticity analysis (5°–11°N, 48°–31°W) for a particular field (in this case, D033.48). The vertical velocity eigenfunctions were then converted to pressure perturbation eigenfunctions $\hat{p}_n$ by calculating the vertical gradient of $\hat{w}_n$; that is,

$$\hat{p}_n = d\hat{w}_n/dz.$$

The modal amplitudes and the reconstructed velocities associated with each mode were then calculated from the pressure perturbation eigenfunctions.

The modal amplitudes are found by vertically integrating the product of the velocity and the pressure perturbation eigenfunction over the depth of the model ocean. This value is then divided by the ocean depth H, which is the deepest level of the CME model (5500 m). There are, however, locations in the region of interest where the topography is shallower than this depth. The velocities at the deeper levels of the model are insignificant in comparison to the values near the surface; hence their contribution to the integral is unlikely to be important. Consequently, the amplitudes calculated from velocity profiles in shallower depths (4500 m) and those obtained from profiles with the same structure in maximum depth waters are unlikely to differ greatly.

Another assumption inherent in a modal decomposition is that there are negligible nonlinear fluid accelerations (Kundu et al. 1975). The mean currents for D033.48, in the region where the vorticity analysis and modal decompositions were performed, are no more than 0.1 m s^{-1} in each of the top four model layers. In the surface layer, the zonal-mean current is 0.04 m s^{-1} to the west. Proehl (1990), when investigating the propagation of waves in the presence of shear, discussed the effects of small amplitude mean flow. He suggested that in this limit, the structure of the resulting wave field may be dominated by wave modes nearby in dispersion space to those calculated from the zero mean background flow. Since the mean flow here is so small, it is reasonable to assume that the structures of the calculated modes are insignificantly different to those calculated in an ocean with no mean background flow.

The values of the eigenvalues, c_n, are 2.34, 1.44, and 0.83 m s^{-1} for $n = 1, 2, 3$, respectively. The values of the internal Rossby radius of deformation R_n for these modes are 115, 71, and 41 km. The R_1 value compares well with the value of 124 km reported by Emery et al. (1984) for this region, while the c_1 value, which can be found using $c_n = f_0 R_n$, is 2.2 m s^{-1} at 7°N.

The meridional (v) and zonal (u) components of velocity at 92 m from the D033.48 field were each decomposed into modes over the region 5° to 11°N, 48° to 31°W. Each of the reconstructed velocity fields associated with the barotropic and first three baroclinic modes were subjected to the vorticity analysis. The leading balance for the $n = 1$ case (Fig. 14) is that representing baroclinic Rossby waves. Similar to the undecomposed case, alternating bands of highs and lows are seen in the $\mathbf{u}_H \cdot \nabla\zeta$, βv, and ζ_t maps in the region through which the waves propagate. The $\mathbf{u}_H \cdot \nabla\zeta$ term dominates the balance as in the undecomposed case; this term is again dominated by $u\partial\zeta/\partial x$. The stretching term is less coherent and its contribution is smaller than the other three terms. The remaining terms of the equation were negligible in comparison to the leading terms. The maps for the $n = 2$ case indicate the same leading balance as the $n = 1$ case (not shown); however, the stretching term is contributing a little more in this case. The magnitudes of the leading terms are similar for both cases.

All the terms for the $n = 3$ case are negligible in comparison to the terms obtained for the first and second modes. No Rossby wave balance is seen in this case. In the barotropic case, $n = 0$, the dominant terms in the oscillation region are βv and ζ_t; this balance of

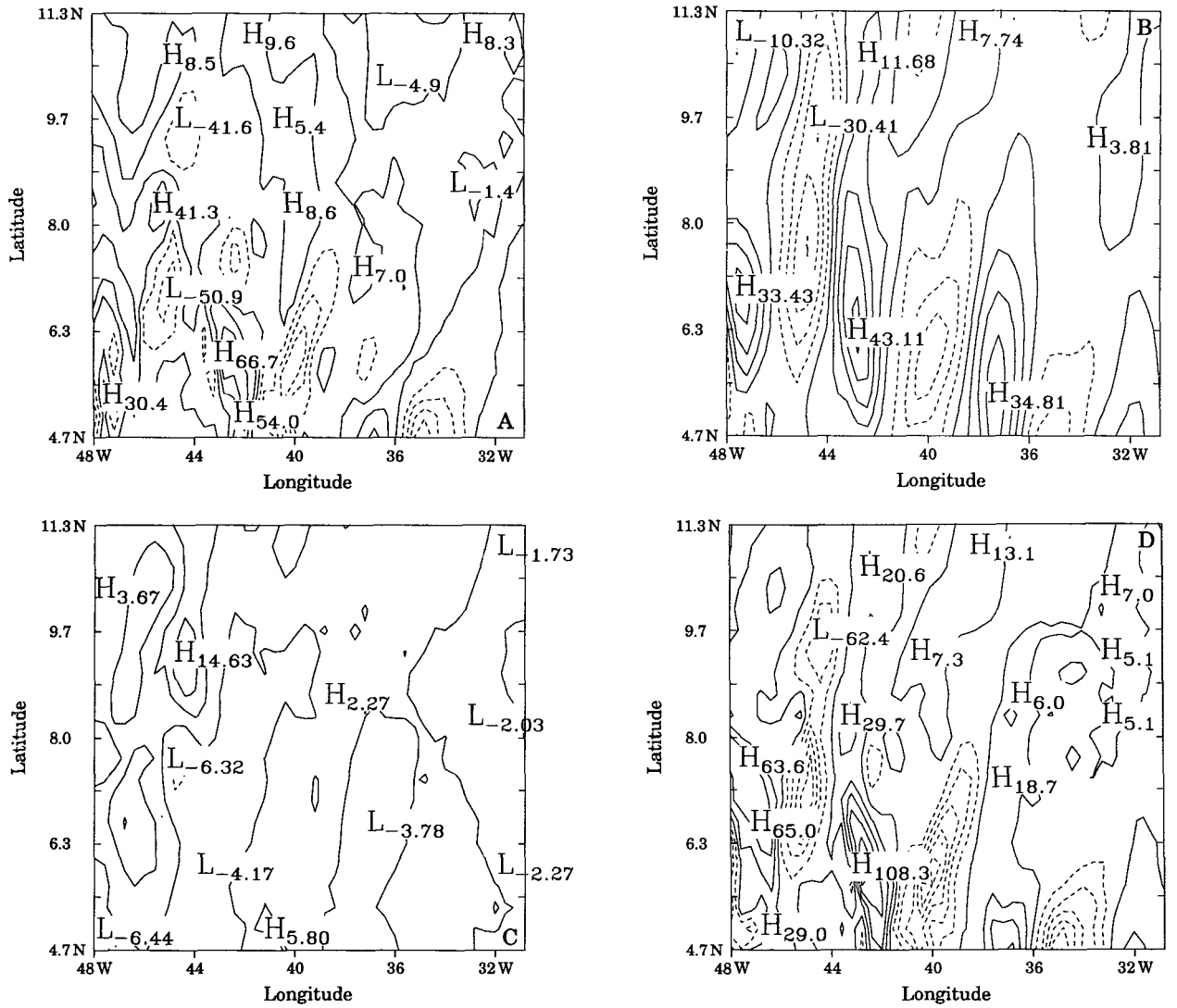

FIG. 14. Same as Fig. 12 except for the $n = 1$ mode.

terms represents barotropic Rossby waves. Horizontal advection of relative vorticity is insignificant.

These vorticity analyses yielded leading balances in the region of the oscillations that represent barotropic and first and second mode baroclinic Rossby waves. To verify that the modal decomposition did not filter out a significant process, the velocity fields associated with the first and second baroclinic modes and the barotropic mode were summed and the vorticity analysis repeated. The leading terms had similar magnitudes to those in the undecomposed case, verifying that no other major process was lost due to the modal decomposition. The spatial patterns of the terms have the advantage over the undecomposed case of being less noisy and the wave patterns are more easily identifiable.

Having proved that the 50-day oscillations are primarily first and second mode baroclinic Rossby waves, the question remains as to their cause. The time history of the meridional velocity contours suggested that they arose from the standing meander pattern of the NECC when the flow of this current slowed. To determine if this is likely, the leading balances of the terms in the vorticity equation were sought when the NECC is fully active. If balances representing baroclinic Rossby waves are found, it would be reasonable to suggest that the 50-day oscillations observed after the disappearance of the NECC are the same waves, only advected westward rather then eastward. A modal decomposition cannot be performed in this case, as the mean eastward current in the November (D319.59) snapshot is about 0.25 m s^{-1}. Such current magnitudes have been characterized by McPhaden et al. (1982) as relatively strong; hence it is no longer possible to disregard the mean background flow in the small amplitude limit.

The dominant terms in this case were seen in the retroflection and meander region of the NECC. The leading balance represents baroclinic Rossby waves (Fig. 15). The dominant balance indicates that baroclinic waves are present in the standing meander region. Horizontal advection of relative vorticity, which is mainly due to $u\partial\zeta/\partial x$, is again the dominant term. Here, the flow is eastward due to the NECC; hence the waves are advected eastward. The scenario suggested above, therefore, quite possibly explains the cause of the 50-day oscillations.

5. Discussion

Findings in the last section, strongly suggest that 50-day oscillations originate from the westward advection of vorticity anomalies left over by the NECC. This scenario will be discussed shortly in the light of the analytic solutions obtained by Campos and Olson (1991). In the Indian Ocean, these oscillations have been attributed to wind forcing or barotropic instability; the likelihood of either being responsible in the CME model will also be discussed. The results from this study will then be compared with those in the Atlantic and those obtained from modeling and observational studies in the Indian Ocean.

Earlier it has been suggested that the 50-day oscillations are westward advected residuals of the NECC meanders. Campos and Olson (1991) obtained a solution from their analytical model that could represent the NBC retroflection and the meandering NECC. The solution contained Rossby waves with amplitude constant in time, decaying spatially. Since the source of these waves was the western boundary region, waves with eastward group velocity, were superimposed on a eastward flowing, westward boundary current extension. The NECC can be viewed as an extension of the retroflecting NBC; hence this solution can be thought of as simulating the NECC meanders. The 50-day oscillations, which are baroclinic Rossby waves with very slow eastward group velocity, appear as the NECC breaks down. They are advected westward by the flow and decay by the end of April. Since the nature of the NECC meanders and the 50-day oscillations is the same, it is reasonable to conclude that they are the same phenomenon. The vorticity analysis confirms this idea in some detail: the meanders are baroclinic Rossby waves, very similar to the 50-day oscillations.

These findings, together with the time history of the flow point to the following scenario regarding the 50-day oscillations. It begins roughly in July with the retroflecting NBC (Fig. 2a) producing Rossby waves with very slow eastward group velocity near the western boundary, which are limited to this western boundary region (Fig. 2b). The NECC then becomes stronger by August (Fig. 3a) and the waves have penetrated to the interior of the basin (35°W) due to eastward advection by the NECC (Fig. 3b), where they dissipate. A stationary Rossby wave pattern is established for several months, while the NECC is active. In December, the NECC starts to slow (Fig. 4a) and the waves retreat westward (Fig. 4b). Hence, the meander pattern is slowly released as the NECC slows. By February the NECC has largely disappeared (Fig. 5a), but the leftover waves are pronounced, retreating westward with the flow (Fig. 5b). By April, the waves have almost entirely disappeared. In May they are absent (Fig. 6b) and the zonal flow is mainly to the west (Fig. 6a). In June, the NECC starts up again and the whole process is repeated.

Observational studies in the Indian Ocean have pointed to the 40–50 day oscillation of the wind field in the lower troposphere discovered by Madden and Julian (1972) as a possible cause of these oscillations. The CME model is forced with climatological mean monthly winds; hence little wind energy in the 40–60 day period is contained in the model forcing. So, although the oscillations could be produced by wind forcing at the periods of the Madden–Julian oscillation in the real ocean, it is not possible in this model.

For the same reason Kindle and Thompson (1989) disregarded wind forcing as the cause of 50-day oscillations in their reduced-gravity layer model. Rather, they attributed the oscillations to barotropic instability resulting from the onset of westward flow as the standing meander pattern of the East African Coastal Current broke down. We investigated barotropic instability as a possible cause of the 50-day oscillations in the CME fields using the same approach employed by Cox (1980) when studying 20–30 day waves. A necessary condition for barotropic instability is that the gradient of absolute vorticity, $\beta - \partial^2 u/\partial y^2$, change sign. This quantity was calculated using temporally averaged zonal velocities for spring (January–April), since this time interval incorporates the period during which westward flow appears. Cox (1980) stated that the existence of a sign change in temporally averaged data is a sufficient but not necessary condition for the existence of a sign change at some point in time within the averaging limits. Meridional sections (5°S–15°N) were constructed through the region of interest (30°–50°W) at 5° intervals. No sign change was seen in any of the meridional sections north of 3°N. The sign change at this latitude is no doubt that observed by Cox (1980) and others explaining the generation of 20–30 day waves. Fifty-day oscillations, however, occur where the necessary condition for barotropic instability is absent. Hence, the underlying cause of the two sets of oscillations are different and barotropic instability is not responsible for the generation of 50-day oscillations. Since Kindle and Thompson (1989) did not test their hypothesis, it is quite possible that the scenario suggested in this study could be equally valid in the Indian Ocean. The standing meander pattern associated with the East African Coastal Current in Kindle and

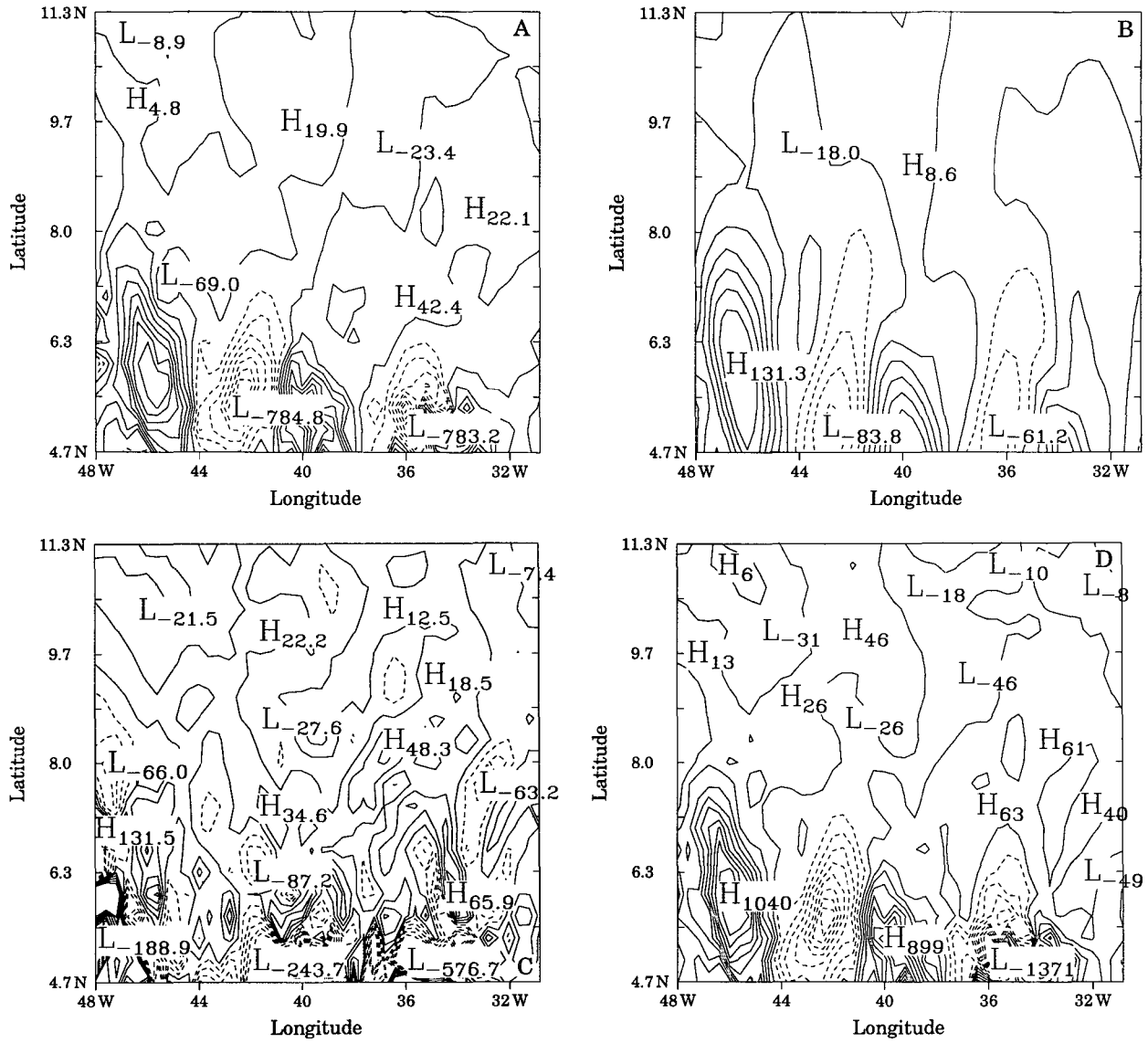

FIG. 15. Leading balance of terms from full vorticity equation: (a) $\mathbf{u}_H \cdot \nabla\zeta$, (b) βv, (c) fw_z, and (d) ζ_t, for November (D319.59) at 92 m. Units are the same as Fig. 12.

Thompson's model breaks down in April, and 50-day oscillations, presumably Rossby waves, appear. There is every reason to believe that the processes seen in the CME model also occurs in theirs.

The properties of the 50-day oscillations seen in the CME model are very similar to those observed by Johns et al. (1990). One notable difference however, is that Johns et al. (1990) found oscillations of periods between 40 and 60 days in the meridional component of velocity of the NBC region throughout the year, whereas they are only present in the CME model from December through April. It is not particularly surprising that Rossby waves near the coast are excited by different mechanisms. The wind forcing used in the CME model lacks the high-frequency components that may be responsible. Also topographic features reflected in the model geometry may be efficient generators of short Rossby waves in the NBC.

The scenario proposed in this paper has been used to explain the 50-day oscillations seen in the model fields. Wind forcing and barotropic instability are not considered to be responsible for the oscillations. Questions remain regarding the reason for the 50-day periodicity and the mechanism responsible for the initial 50-day signal near the western boundary at the onset of the retroflection period seen in Fig. 10. It is possible that the latter signal is related to the quasi-periodic 50-day pulsation of the NBC retroflection front between

6° and 10°N, suggested by Johns et al. (1990) to be responsible for eddy shedding. It may be possible that one of these quasi-periodic frontal pulses, generated by an instability of the NBC system, produces Rossby waves that are advected eastward by the NECC. Hence, the observed 50-day periodicity may be indirectly related to the periodicity of the frontal movement.

6. Conclusions

The behavior, nature, and dynamics of 50-day oscillations were investigated in the western tropical region of the CME general circulation model. These oscillations were seen in the meridional component of velocity between 5° and 11°N, 35° and 55°W. They occur between December and April and their onset coincides with the seasonal break down of the meander pattern of the NECC. They appear first near 5°N, 36°W and are advected westward. They have a westward phase speed of about 0.1 m s^{-1}, a wavelength of about 600 km, and a very slow eastward group velocity. Their period, phase speed, and wavelength agree with observations (Johns et al. 1990).

Calculation of the leading balance of terms from the full vorticity equation in the region where the oscillations occur, following a modal decomposition, showed that the oscillations were first and second mode baroclinic Rossby waves. Repetition of the vorticity analysis during the retroflection period revealed the NECC meanders to be baroclinic Rossby waves; the same as the 50-day oscillations. These findings, together with the time evolution of the flow field over an annual cycle, suggested that the 50-day oscillations were the westward advected residue of the NECC meander pattern that is released as the NECC slows in fall. Neither wind forcing or barotropic instability were considered to be responsible for the oscillations.

This study represents a contribution to the growing body of literature attempting to explain the nature and causes of 50-day oscillations. It was performed over adequate temporal and spatial scales; hence, complements observational studies performed with spatially limited data. Understanding the behavior and dynamics of these oscillations is important to our understanding of low-latitude western boundary currents such as the NBC system. Information obtained from this study could be used in both future modeling and observational studies of this and other low-latitude western boundary currents. Data collection strategies could be guided by these findings. Spectra of the current meter data collected by Richardson and Reverdin (1987) at 6°N, 28°W display a significant peak at 50 days. Hence, several current meter arrays could be placed along the path where the waves were advected. The description and dynamics found in the model could then be validated in the ocean interior. As well, the importance of the high frequency wind forcing could be assessed by collecting concurrent wind data. The role of this wind forcing could also be evaluated in a global general circulation model forced with daily wind fields.

Acknowledgments. This research was sponsored by the National Science Foundation under Contract OCE-89-22860. The authors thank Gabriel Csanady for his considerable input into this project, both in terms of insight and time. Michael Spall provided the vorticity code and helpful comments. The anonymous reviewers are thanked for their time and input.

REFERENCES

Böning, C. W., and F. A. Schott, 1993: Deep currents and the eastward salinity tongue in the equatorial Atlantic: Results from an eddy-resolving, primitive equation model. *J. Geophys. Res.*, **98,** 6991–6999.

Boyd, J. D., 1986: Thermohaline steps off the northeast coast of South America, Ph.D. thesis, Texas A&M University, 171 pp.

Bryan, F. O., and W. R. Holland, 1989: A high resolution simulation of the wind- and thermohaline driven circulation in the North Atlantic Ocean. *'Aha Huliko'a Parameterization of Small-Scale Processes,* P. Muller and D. Henderson, Eds., Hawaii Institute of Geophysics, 99–115.

——, C. W. Böning, and W. R. Holland, 1994: On the mid-latitude circulation in a high-resolution model of the North Atlantic. *J. Phys. Oceanogr.*, **24,** 289–305.

Byran, K., 1969: A numerical method for the study of the circulation of the World Ocean. *J. Comput. Phys.*, **4,** 347–376.

Campos, E. J. D., and D. B. Olson, 1991: Stationary Rossby waves in western boundary current extensions. *J. Phys. Oceanogr.*, **21,** 1202–1224.

Cox, M. D., 1980: Generation and propagation of 30–day waves in a numerical model of the Pacific. *J. Phys. Oceanogr.*, **10,** 1168–1186.

——, 1984: A primitive equation three dimensional model of the ocean. GFDL Ocean Group Tech. Rep. No. 1, Geophysical Fluid Dynamics Laboratory/NOAA, 250 pp.

Didden, N., and F. A. Schott, 1992: Seasonal variations in the western tropical Atlantic: Surface circulation from Geosat Altimetry and WOCE model results. *J. Geophys. Res.*, **97,** 3529–3541.

——, and ——, 1993: Eddies in the North Brazil Current retroflection region observed by Geosat altimetry. *J. Geophys. Res.*, **98,** 20 121–20 131.

Emery, W. J., and J. S. Dewar, 1982: Mean temperature–salinity, salinity–depth and temperature–depth curves for the north Atlantic and the north Pacific. *Progress in Oceanography,* Vol. 11, Pergamon 219–305.

——, W. G. Lee, and L. Magaard, 1984: Geographic and seasonal distribution of Brunt–Väisälä frequency and Rossby radii in the north Pacific and north Atlantic. *J. Phys. Oceanogr.*, **14,** 294–317.

Gill, A. E., 1982: *Atmosphere–Ocean Dynamics.* Academic Press, 662 pp.

Han, Y. J., 1984: A numerical world ocean general circulation model. Part II: A baroclinic experiment. *Dyn. Atmos. Oceans,* **8,** 141–172.

Hellerman, S., and M. Rosenstein, 1983: Normal monthly wind stress over the world ocean with error estimates. *J. Phys. Oceanogr.*, **13,** 1093–1104.

Hénin, C., and P. Hisard, 1987: The North Equatorial Countercurrent observed during the Programme Océan et Climate Dans l'Atlantique equatorial experiment in the Atlantic Ocean, July 1982 to August 1984. *J. Geophys. Res.*, **92,** 3751–3758.

——, ——, and B. Piton, 1986: FOCAL, Vol. 1, Observations hydrologiques dans l'Océan Atlantique Equatorial (juillet 1982–août 1984), *Editons de l'ORSTOM Collect. Trav. et Doc.*, ORSTOM, **196,** 191 pp.

Johns, W. E., T. N. Lee, F. A. Schott, R. J. Zantoff, and R. H. Evans, 1990: The North Brazil Current retroflection: Seasonal structure and eddy variability. *J. Geophys. Res.*, **95,** 22 103–22 120.

Katz, E. J., R. L. Molinari, D. E. Cartwright, P. Hisard, H. U. Lass, and A. deMesquita, 1981: The seasonal transport of the Equatorial Undercurrent in the western Atlantic (during the Global Weather Experiment). *Oceanol. Acta,* **4,** 445–450.

Kindle, J. C., and J. D. Thompson, 1989: The 26–day and 50–day oscillations in the western Indian Ocean: Model results. *J. Geophys. Res.*, **94,** 4721–4736.

Kraus, E. B., and J. S. Turner, 1967: A one-dimensional model of the seasonal thermocline: Part II: The general theory and its consequences. *Tellus,* **19,** 98–106.

Kundu, P. K., J. S. Allen, and R. L. Smith, 1975: Modal decomposition of the velocity field near the Oregon coast. *J. Phys. Oceanogr.*, **5,** 683–704.

Legeckis, R., 1977: Long waves in the eastern equatorial Pacific Ocean: A view from a geostationary satellite. *Science,* **197,** 1179–1181.

Levitus, S., 1982: *Climatological Atlas of the World Ocean.* NOAA Prof. Paper, No. 13, 173 pp.

Madden, R. A., and P. R. Julian, 1972: Description of global-scale circulation cells in the tropics with a 40–50 day period. *J. Atmos. Sci.*, **29,** 1109–1123.

McPhaden, M. J., 1982: Variability in the central equatorial Indian Ocean. Part I: Ocean dynamics. *J. Mar. Res.*, **40,** 157–176.

Mysak, L. A., and G. J. Mertz, 1984: A 40- to 60-day oscillation in the source region of the Somali Current during 1976. *J. Geophys. Res.*, **89,** 711–715.

Pedlosky, J., 1987: *Geophysical Fluid Dynamics.* 2d. ed. Springer-Verlag, 710 pp.

Philander, S. G. H., W. J. Hurlin, and R. C. Pacanowski, 1986: Properties of long equatorial waves in models of the seasonal cycle in the tropical Atlantic and Pacific Oceans. *J. Geophys. Res.*, **91,** 14 207–14 211.

Pinardi, N., and A. R. Robinson, 1986: Quasigeostrophic energetics of open ocean regions. *Dyn. Atmos. Oceans,* **10,** 185–219.

——, and ——, 1987: Dynamics of deep thermocline jets in the POLYMODE region. *J. Phys. Oceanogr.*, **17,** 1163–1188.

Proehl, J. A., 1990: Equatorial wave–mean flow interaction: The long Rossby waves. *J. Phys. Oceanogr.*, **20,** 274–294.

Quadfasel, D. R., and J. C. Swallow, 1986: Evidence for 50–day period planetary waves in the South Equatorial Current of the Indian Ocean. *Deep-Sea Res.*, **33,** 1307–1312.

Richardson, P. L., and T. K. McKee, 1984: Average seasonal variation of the Atlantic equatorial currents from historical ship drifts. *J. Phys. Oceanogr.*, **14,** 1226–1238.

——, and G. Reverdin, 1987: Seasonal cycle of velocity in the Atlantic North Equatorial Countercurrent as measured by surface drifters, current meters, and ship drifts. *J. Geophys. Res.*, **92,** 3691–3708.

Schott, F. A., and C. W. Böning, 1991: The WOCE model in the western tropical Atlantic: Upper layer circulation. *J. Geophys. Res.*, **96,** 6993–7004.

——, M. Fieux, J. Kindle, J. Swallow, and R. Zantopp, 1988: The boundary currents east and north of Madagascar Part 2: Direct measurements and model comparisons. *J. Geophys. Res.*, **93,** 4963–4974.

Spall, M. A., 1989: Regional primitive equation modeling and analysis of the POLYMODE data set. *Dyn. Atmos. Oceans,* **14,** 125–174.

——, 1990: Circulation in the Canary basin: A model/data analysis. *J. Geophys. Res.*, **95,** 9611–9628.

——, 1992: Rossby wave radiation in the Cape Verde frontal zone. *J. Phys. Oceanogr.*, **22,** 796–807.

Stammer, D., and C. W. Böning, 1992: Mesoscale variability in the Atlantic Ocean from Geosat altimetry and WOCE high-resolution numerical modeling. *J. Phys. Oceanogr.*, **22,** 732–752.

Swallow, J., M. Fieux, and F. Schott, 1988: The boundary currents east and north of Madagascar Part 1: Geostrophic currents and transports. *J. Geophys. Res.*, **93,** 4951–4962.

——, F. Schott, and M. Fieux, 1991: Structure and transport of the East African Coastal Current. *J. Geophys. Res.*, **96,** 22 245–22 257.

Weisberg, R. H., and T. J. Weingartner, 1988: Instability waves in the equatorial Atlantic Ocean. *J. Phys. Oceanogr.*, **18,** 1641–1657.